crystals

MDPI

Article

Designing of WS_2@NiCoS@ZnS Nanocomposite Electrode Material for High-Performance Energy Storage Applications

Muhammad Imran [1], Amir Muhammad Afzal [1,*], Areej S. Alqarni [2], Muhammad Waqas Iqbal [1] and Sohail Mumtaz [3]

[1] Department of Physics, Riphah International University, Lahore Campus, Lahore 54000, Pakistan; m.imransharif24@gmail.com (M.I.); waqas.iqbal@riphah.edu.pk (M.W.I.)
[2] Department of Physics, College of Science, Princess Nourah Bint Abdulrahman University, P.O. Box 84428, Riyadh 11671, Saudi Arabia; arsalqarni@pnu.edu.sa
[3] Department of Electrical and Biological Physics, Kwangwoon University, Seoul 01897, Republic of Korea; sohail.ahmed2015@gmail.com
* Correspondence: amirafzal461@gmail.com

Abstract: Researchers are developing innovative electrode materials with high energy and power densities worldwide for effectual energy storage systems. Transition metal dichalcogenides (TMDs) are arranged in two dimensions (2D) and have shown great promise as materials for photoelectrochemical activity and supercapacitor batteries. This study reports on the fabrication of WS_2@NiCoS and WS_2@NiCoS@ZnS hybrid nano-architectures through a simple hydrothermal approach. Because of the strong interfacial contact between the two materials, the resultant hierarchical hybrids have tunable porosity nanopetal decorated morphologies, rich exposed active edge sites, and high intrinsic activity. The specific capacities of the hybrid supercapacitors built using WS_2@NiCoS and WS_2@NiCoS@ZnS electrodes are 784.38 C g^{-1} and 1211.58 C g^{-1} or 2019.3 F g^{-1}, respectively, when performed at 2 A g^{-1} using a three-electrode setup. Furthermore, an asymmetric device (WS_2@NiCoS@ZnS//AC) shows a high specific capacity of 190.5 C g^{-1}, an energy density of 49.47 Wh $kg^{-1,}$ and a power density of 1212.30 W kg^{-1}. Regarding the photoelectrochemical activity, the WS_2@NiCoS@ZnS catalyst exhibits noteworthy characteristics. Our findings pave the way for further in-depth research into the use of composite materials doped with WS_2 as systematic energy-generating devices of the future.

Keywords: tungsten disulfide (WS_2); zinc sulfide (ZnS); active redox sites; photoelectrochemical activity; electrode material; energy storage

check for updates

Citation: Imran, M.; Afzal, A.M.; Alqarni, A.S.; Iqbal, M.W.; Mumtaz, S. Designing of WS_2@NiCoS@ZnS Nanocomposite Electrode Material for High-Performance Energy Storage Applications. *Crystals* **2024**, *14*, 916. https://doi.org/10.3390/cryst14110916

Academic Editor: Kaveh Edalati

Received: 2 October 2024
Revised: 18 October 2024
Accepted: 21 October 2024
Published: 24 October 2024

Copyright: © 2024 by the authors. Licensee MDPI, Basel, Switzerland. This article is an open access article distributed under the terms and conditions of the Creative Commons Attribution (CC BY) license (https://creativecommons.org/licenses/by/4.0/).

1. Introduction

The energy issue and the need for electricity have gained prominence due to social improvements. Thus, developing novel electrode materials has received a lot of interest in energy-efficient transformation and storage [1,2]. Electrochemical capacitors (ECs) are experiencing a growing demand, particularly for cutting-edge, flexible, electrochemical energy storage technologies that are portable and wearable [3,4]. ECs possess numerous mandatory features compared to lithium/sodium ion or solid-state batteries. These include durable cycle stability, high specific capacitance, quick charge/discharge capability, remarkable power density, and safe operation at a reasonable cost. Due to their low energy density, extensive efforts have been dedicated to enhancing their intrinsic properties. This involves modifying electrode designs, expanding the surface area, creating electrodes with excellent electrical and ionic conductivity, and creating mechanically and chemically robust interfaces [5,6].

Transition metal dichalcogenides (TMDs) have advanced significantly because of their superb catalytic activity in electrochemical applications, affordability, and terrestrial abundance [7–10]. TMD has a triple-layer packing arrangement with a thickness ranging from

6 to 7 Å that is weakly connected to neighboring layers by van der Waals forces [11,12]. Molybdenum sulfides (MoS_2) and tungsten sulfides (WS_2) are two examples of metal sulfide TMD structures with a hexagonally packed structure resembling graphite. In this configuration, covalent bonding is used to introduce metal layers between two sulfur layers. Because MoS_2 and WS_2 have a huge specific surface area, many sulfur-active facets, and multivalent oxidation states of transition metal ions, they may transfer and accumulate charges efficiently [13,14]. Pure WS_2-based electrochemical devices cannot be further improved due to the limited exposure of active sites and their inherent semiconducting nature [15,16]. Recently, numerous studies have focused on enhancing the number of active facets in WS_2 through doping with heteroatoms, creating defects/vacancies, designing various crystal phases and morphologies, and tuning the active area [17–19]. Hence, developing electrode materials exhibiting high active facets oriented toward edges/defects represents a promising approach for hydrogen production and energy storage [20,21]. Apart from the mechanism for storing charges, the presentation of the device is also influenced by the electrode material. The fundamental qualities of an ideal positive electrode material for supercapattery include porous structure, excellent conductivity, and electroactivity [22,23]. Transition metal phosphides, oxides, and sulfides are appropriate materials for positive electrodes [24–26]. Transition metal sulfides' robust electroactivity and chemical stability make them highly suitable electrode materials [25,27]. For example, Rauf et al. documented the electrochemical analysis of ZnS nanowires deposited on nickel foil. The ZnS electrode demonstrated a specific capacity (Qs) of 81 F g^{-1} at 0.5 A g^{-1} [28]. The ZnS electrode confirmed an energy density (E_d) of 51 Wh kg^{-1} at a power density (P_d) of 200 W kg^{-1}, sustaining cyclic stability of 87% after 10,000 charge–discharge cycles. Wan and collaborators hydrothermally synthesized cobalt sulfide (CoS) nanotubes, revealing a Qs of 285 F g^{-1} at 0.5 A g^{-1} with 99% cyclic stability. The collaborative impact of both ZnS and CoS enhanced the electrode performance, as evidenced by the ZnS/CoS binary composite developed by Chameh et al., which displayed an exceptional Qs of 1646 F g^{-1} at 1 A g^{-1} [29]. The combination of ZnS and CoS in the composite resulted in an E_d of 39.41 Wh kg^{-1} paired with a P_d of 7080 W kg^{-1} while maintaining 89.0% capacitance retention in an asymmetry device. Furthermore, Wang et al. reported synthesizing a ternary metal sulfide electrode in which three transition metals combined to form $NiCoMnS_4$ produced an extraordinary Qs of 2470.40 F g^{-1} at 1 A g^{-1} [30]. The synthesis method is crucial, as it significantly influences the electrochemical capabilities and performance of nanomaterials. For example, CoS synthesized through a hydrothermal approach [27] exhibited a Cs value of 506.70 F g^{-1} at 1.5 A g^{-1}. In contrast, CoS synthesized using sonochemical methods, as reported by Iqbal et al., showed a Cs value of approximately 340 F g^{-1} [31]. The 2D TMDs are a new class of positive electrode materials for supercapattery that may be used to attain higher specific energy. These TMDs are composed of two chalcogen atoms (X) and a transition metal atom (M) bound together by covalent bonds to create the structure known as X–M–X. Their inherent layered configuration facilitates the insertion of ions between these layers, facilitating swift ionic diffusion and thereby enhancing their electrochemical performance [32]. TiS_2, MoS_2, WS_2, $MoSe_2$, and WSe_2 are only a few of the TMDs that have remarkable electrochemical performance [33]. The presence of various oxidation states (approximately +2.0 to + 6.0) and a substantial surface area enable 2D materials to undergo electrochemical and electrostatic charge storage processes. This, in turn, results in elevated specific capacitance (Cs) and energy density (Ed) values for the electrode [34,35]. Gupta and colleagues employed hydrothermal synthesis to produce layered MoS_2, which was subsequently subjected to electrochemical testing [36]. The graphene-like configuration resulted in a capacitance (Cs) value of 255 F g^{-1} at 0.25 A g^{-1}, along with an energy density (Ed) of 35.50 Wh k g^{-1} under the same current density. Moreover, the MoS_2 electrode showed remarkable stability across many cycles, exhibiting only a 30% reduction in its original capacitance. WS_2, another transition metal dichalcogenide (TMD) with a graphene-like structure, features a layer-to-layer distance of approximately 0.170 nm, facilitating easy intercalation of metal ions and contributing to its outstanding electroactive properties [37].

While TMDs exhibit impressive capacitive characteristics, they often suffer from reduced cyclic stability and conductivity. To address these limitations, researchers enhance these materials by creating hybrid structures of transition metal sulfides, which have proven particularly effective for such combinations. The cyclic stability of WS_2 and CoS was found to be 89.83% and 92.50%, respectively, in research conducted by Krishna et al. This stability was significantly improved to 97.10% when WS_2 was combined with CoS [38]. The electrical resistance values for WS_2 nanorods and Co_3S_4 microspheres were 3.02 Ω and 3.81 Ω, respectively, according to an independent study by Shrivastav et al. Upon combining these materials, the hybrid electrode exhibited a reduced resistance, measuring 2.73 Ω [39].

This study explores a new approach for creating novel hierarchical lamellar WS_2@NiCoS@ZnS hybrid structures using a hydrothermal method. These structures are formed through a solid interfacial interaction between NiCoS@ZnS and WS_2 nanosheets, making them promising alternatives for current requirements. The hybridization process, which results in the WS_2@NiCoS@ZnS hybrid structure, leads to increased interlayer space amid the duos, enhancing intercalation/extraction ion kinetics and stability. The highly conductive WS_2 nanostructures in the hybrid configuration maximize electrical conductance, facilitating rapid electron-transfer kinetics and improving electrical performance at the interfaces between electrodes and active edges. Utilizing WS_2@NiCoS and WS_2@NiCoS@ZnS hybrid structures in assembled devices demonstrates remarkable capabilities in supercapacitors and photoelectrochemical activities. Specifically, supercapattery incorporating WS_2@NiCoS and WS_2@NiCoS@ZnS electrodes exhibit specific capacity of 784.38 C g^{-1} and 1211.58 C g^{-1} or 2019.3 F g^{-1}, respectively, at 2 A g^{-1} in three-electrode measurements. In supercapattery WS_2@NiCoS//AC and WS_2@NiCoS@ZnS//AC devices, specific capacities of 145.93 and 190.5 C g^{-1} are achieved, respectively, at 1.5 A g^{-1}, providing an energy density of 49.47 Wh kg^{-1} at a power density of 1212.30 W kg^{-1}. This supercapattery device (WS_2@NiCoS@ZnS//AC) shows high cyclic stability, columbic efficiency of 93.23%, and capacity retention of 85.19% after 5000 GCD cycles. These results show that the suggested material composition is suitable for applications using supercapattery energy storage devices.

2. Experimental Section

Nanomaterials for supercapattery technology are produced utilizing nickel nitrate hexahydrate ($Ni(No_3)_2.6H_2O$), cobalt (II) nitrate hexahydrate ($Co(NO_3)_2.6H_2O$), sodium sulfide, hydrate ($Na_2S.nH_2O$), tungsten sulfide (WS_2), zinc sulfide (ZnS), lithium nitrate ($LiNO_3$), potassium hydroxide (KOH), and N-methyl 2-pyrrolidone (NMP) obtained from Sigma-Aldrich. N-polyvinylidene-fluoride (PVDF) and carbon black are obtained from MERCK. The WS_2 powder is needed for the manufacture of WS_2 nanosheets. WS_2 nanosheets are synthesized using the tip-sonication technique, which uses an ultrasonic probe. A surgical HUT 80-1 centrifuge machine is used for material collection and cleaning. To produce WS_2 nanosheets with controlled thickness and size distribution, which are advantageous for applications such as electronics, catalysis, and energy storage, the tip-sonication method is scalable and efficient [40,41].

2.1. Synthesis of NiCoS@ZnS

The NiCoS nanocomposite was synthesized using a hydrothermal technique. Considering this, we have created three solutions: $Ni(NO_3)_2.6H_2O$ (0.3 M) (purity 98%), $Co(NO_3)_2.6H_2O$ (0.3 M) (purity 99.8%), and $Na_2S.nH_2O$ (0.4 M) (purity 99.9%) were mixed individually in 50 mL deionized (DI) water. The obtained mixture was heated at 170 °C for 12 h. NiCoS precipitous was collected and centrifuged at 3000 rpm. The recovered samples were extensively cleaned with DI water and ethanol to remove leftover pollutants. Figure 1 shows a schematic of the synthesis process of WS_2 nanosheets, deposition, and electrode testing steps of the electrode. We prepared NiCoS@ZnS by physical blending of 80/20 wt.%

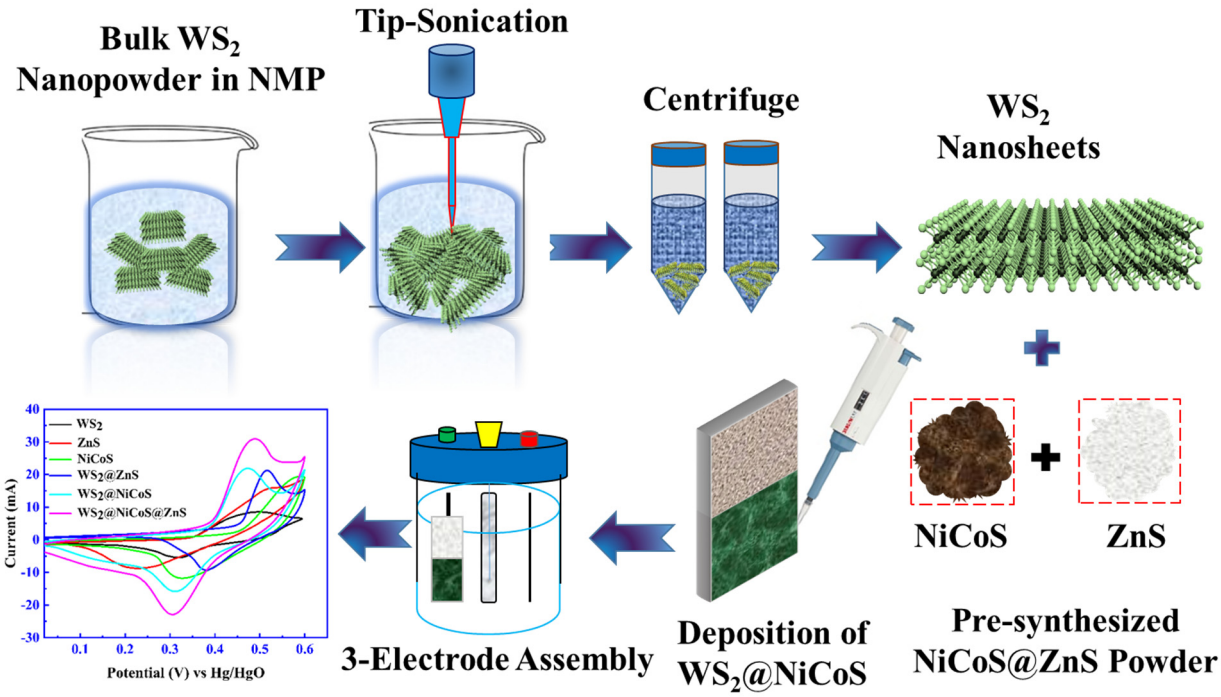


Figure 1. A graphic illustration showing the synthesis process, deposition, and electrode testing steps of WS_2@NiCoS@ZnS.

2.2. Synthesis of WS_2@NiCoS@ZnS Nanocomposite

In a 50 mL mixture of NMP solvent, 6 g of pure WS_2 powder is mixed. A probe sonicator is used to sonicate the mixture for 3 h. Centrifuging the sonicated WS_2/NMP combination at 1500 rpm for 3.5 h yields the dispersed WS_2 nanosheet solution. Using a mortar and pestle, a 5 wt% mixture of WS_2 nanosheet powder and NiCoS@ZnS is prepared. Figure 1 is a simplified flow diagram showing the steps involved in creating WS_2 nanosheets, WS_2@NiCoS@ZnS, and characterizing the final product. The electrode slurry is made up of active material (80%), carbon black (10%), and PVDF binder (10%). After stirring the ingredients in a slurry tube all night, the resulting homogeneous slurry was pipetted over the nickel foam. Properly cleansing and washing the nickel foam (NF) with HCL, ethanol, and DI water is preceded for deposition. The electrolyte slurry is deposited on a 1 × 1 cm^2 area of nickel foam, with 5 mg of the deposited material. An electrochemical test using a 1.0 M KOH electrolyte is performed on the dried WS_2@NiCoS@ZnS electrode.

3. Results and Discussion

Characterization Techniques

Crystalline quality and phase purity of WS_2@NiCoS@ZnS were investigated using XRD. The perceived sharp peaks assert the presence of crystalline WS_2, ZnS, NiCoS@ZnS, NiCoS, WS_2@NiCoS, and WS_2@NiCoS@ZnS, as depicted in Figure 2a. In the case of NiCoS, the XRD peaks at 2θ values of 16.09°, 27.7°, 31.9°, 39.32°, 45.03°, 50.14°, and 55.08°, corresponding to the planes (100), (002), (400), (311), (004), (511), and (440), respectively (JCPDS card No. 23-382) [42–44]. The deflection peaks of hexagonal phase WS_2 in the pattern at 2θ 14.5°, 33.5°, 42.06°, and 61° correspond to (002), (004), (006), and (008) (JCPDS No: 37-1492) [45]. In ZnS, the peak becomes visible at 28.6°, 48.03°, and 65.6°, consistent with the (111), (220), and (311) plane, which serves as evidence for the presence of ZnS [46].

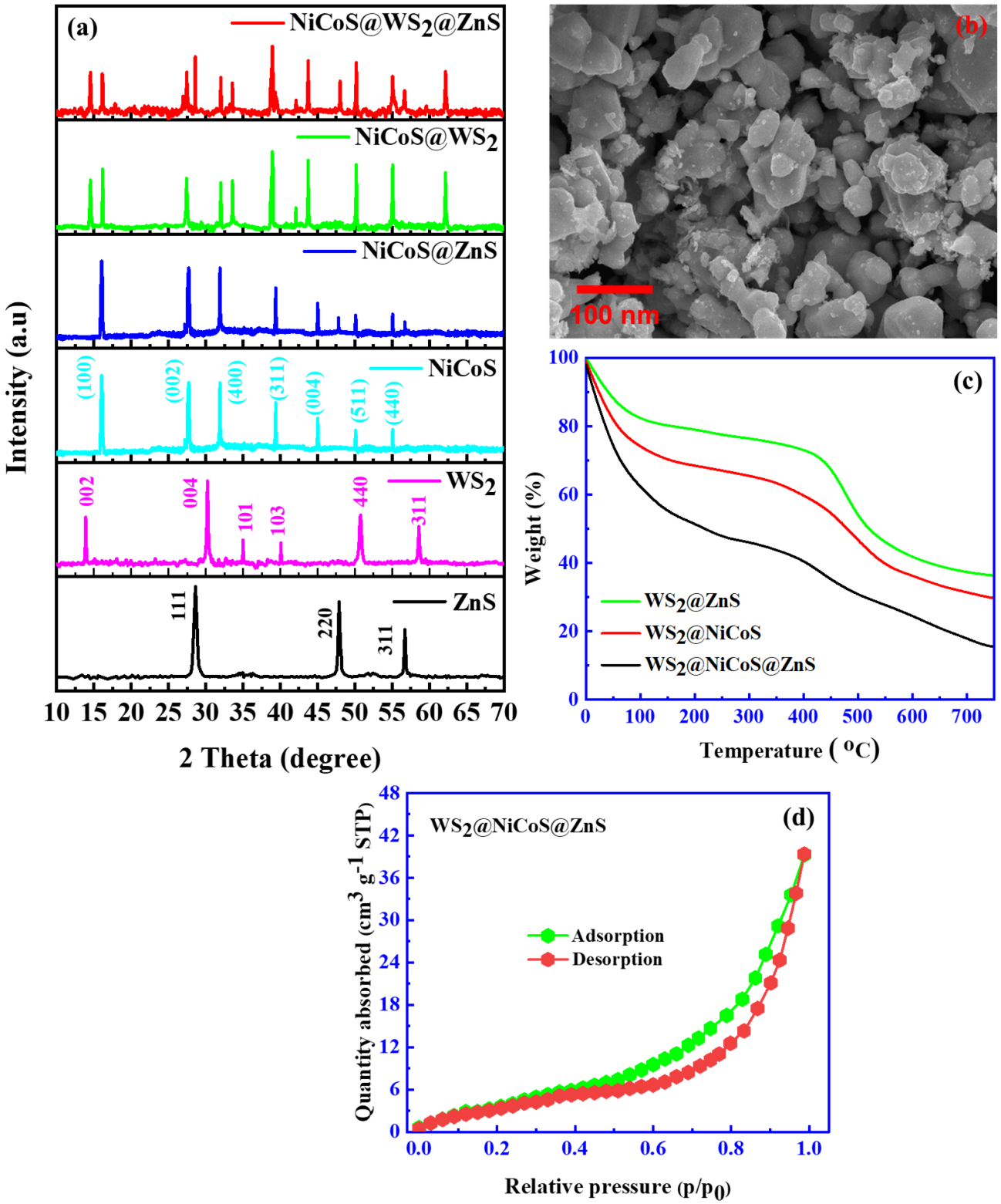


Figure 2. (**a**) XRD investigation of WS_2, ZnS, NiCoS@ZnS, NiCoS, WS_2@NiCoS, WS_2@NiCo, and WS_2@NiCoS@ZnS. (**b**) SEM image of WS_2@NiCoS@ZnS nanocomposite. (**c**) TGA examination for WS_2@ZnS, WS_2@NiCoS, and WS_2@NiCoS@ZnS. (**d**) BET analysis of WS_2@NiCoS@ZnS nanocomposite material.

When choosing the nanomaterial for use in supercapattery, its structure is essential. Electrode material and electrolyte interact well due to the material's surface topography.

According to the claim, the shape of the material affects its capacitive and conductive characteristics [39].

The XRD for NiCoS, NiCoS@ $WS_{2,}$ and NiCoS@WS_2@ZnS is shown in Figure 2a, whereas big particles result from the aggregation of smaller particles and nanosheet stacking. The Figure clearly shows WS_2 nanosheets interspersed throughout the NiCoS@ZnS aggregates. By increasing the material's conductive and capacitive properties, nanosheets make the charging and discharging process easier. In addition to facilitating charge transfer, these nanosheets make additional active sites available for the infusion of metal ions.

The WS_2@NiCoS@ZnS nanocomposite materials' SEM picture is shown in Figure 2b. NiCoS@ZnS nanocomposites that have established excellent contact with WS_2 nanosheets are suggested by the fragments' transparency and few-layer thickness, which are signs of the presence of dopants in the WS_2 hybrid materials [47]. The WS_2 enhanced the pores' area and surface energy and NiCoS@ZnS nanoflakes, which is necessary to store plenty of charge carriers and maintain their transparency [48,49].

Moreover, a thermogravimetric analysis (TGA) test is used to evaluate the material's stability and purity. The skeletons of the treated materials must be visible, which requires TGA analysis. The TGA is performed for the WS_2@ZnS, WS_2@NiCoS, and WS_2@NiCoS@ZnS between 0 and 750 °C to determine the relationship between temperature and weight loss. Figure 2c shows a slight weight loss between 30 to 180 °C. The mass of the pure WS_2@ZnS sample drops dramatically between 200 and 450 °C. It has been observed that the WS_2@NiCoS exhibited a gradual decrease in weight when subjected to temperatures ranging from 200 to 450 °C. This is mainly attributable to the pyrolysis of oxygenated and hydrogenated units [50]. Notably, the WS_2@NiCoS@ZnS composite has a minor weight defeat of 17.22 wt%, considerably smaller than WS_2@ZnS (40%) and WS_2@NiCoS (30%).

The BET estimates the surface area, pore volume, and pore size, which may be controlled to improve the electrode's performance. Additionally, to find out the exact surface areas of the samples, it is used to calculate the adsorption and desorption of nitrogen. The average pore size, surface area, and pore volume of WS_2@ZnS are 33.7 nm, 34.4 m^2 $g^{-1,}$ and ~17.51 cm^3 $g^{-1,}$ respectively (Figure S1a). In the case of WS_2@NiCoS, the pore size, surface area, and pore volume are 27.5 nm, 44.8 m^2 $g^{-1,}$ and ~67 cm^3 g^{-1}, respectively (Figure S1b). Figure 2d shows that WS_2@NiCoS@ZnS has the pore size, surface area, and pore volume of 27.5 nm, 44.8 m^2 $g^{-1,}$ and ~67 cm^3 $g^{-1,}$ respectively. WS_2@NiCoS@ZnS composite has a high surface area-to-volume ratio, which means it can have more adsorption and reactive sites available, which means it can keep its photocatalytic activity [51–54]. According to the findings of the BET study, WS_2@NiCoS@ZnS has a higher surface area, which permits a more substantial anticipation of charges on the electrode surface [55]. High-charge storage capacity and quick ion diffusion are made possible by the composite's enormous surface area and pore volume [56].

X-ray photoelectron spectroscopy (XPS) analysis determines the WS_2@NiCoS@ZnS nanocomposite. As shown in Figure S2a, two XPS spectra of Ni $2P_{3/2}$ and Ni $2P_{1/2}$ were seen with binding energies of 856.7 and 871.5 eV, respectively [57]. This demonstrates that NiCoS has both Ni^{2+} and Ni^{3+} peaks [35]. As seen in Figure S2b, the spectrum investigation of Co2P presented two unique peaks at 778.4 and 793.7 eV, which corresponded to $Co2P_{3/2}$ and Co $2P_{1/2}$, respectively. Here, we may see the existence of Co^{2+} and Co^{3+}. The presence of Zn^{2+} is indicated by two peaks in the Zn 2P spectra, as shown in Figure S2c: one at 1046.5 eV for Zn $2P_{1/2}$, and another one at 1023 eV for Zn $2P_{3/2}$. The orbit splitting for the latter peak is 23.5 eV. As shown in Figure S2d, the presence of sulfur in the composite is confirmed by the S $2P_{3/2}$ peak at 161.0 eV and the S $2P_{1/2}$ peak at 163.6 eV. Figure S2e from the literature shows that the XPS spectra of WS_2 also include peaks of $W4f_{7/2}$, $W4f_{5/2}$, and W $5P_{3/2}$, with binding energies of 32.98 eV, 35.89 eV, and 37.78 eV, respectively, all corresponding to the W in 4^+ form in WS_2 nanosheets [58].

4. Electrochemical Analyses

Electrochemical characterization of the electrode materials begins by recording CV at a constant potential window (PW) of 0 to 0.6 V and different scan rates from 5 mV s^{-1} to 60 mV s^{-1}. The CV comparison of all electrodes (WS_2, ZnS, NiCoS, WS_2@ZnS, WS_2@NiCoS, NiCoS@ZnS, and WS_2@NiCoS@ZnS measured at 5 mV s^{-1} in 1M KOH electrolyte is shown in Figure 3a. The CV profiles with their faradaic peaks in Figure 3b–d represent the battery-grade quality of WS_2@ZnS, WS_2@NiCoS, and WS_2@NiCoS@ZnS, respectively. The redox-active properties of WS_2@NiCoS@ZnS contribute to the higher peak current determined from the CV, as seen in Figure 3d. When we increase the scan rate, there is a noticeable change in the peak currents of both pristine and doped material. This shift might be caused by the high ion mobility rate, which is faster than the faradaic processes and raises the peak currents.

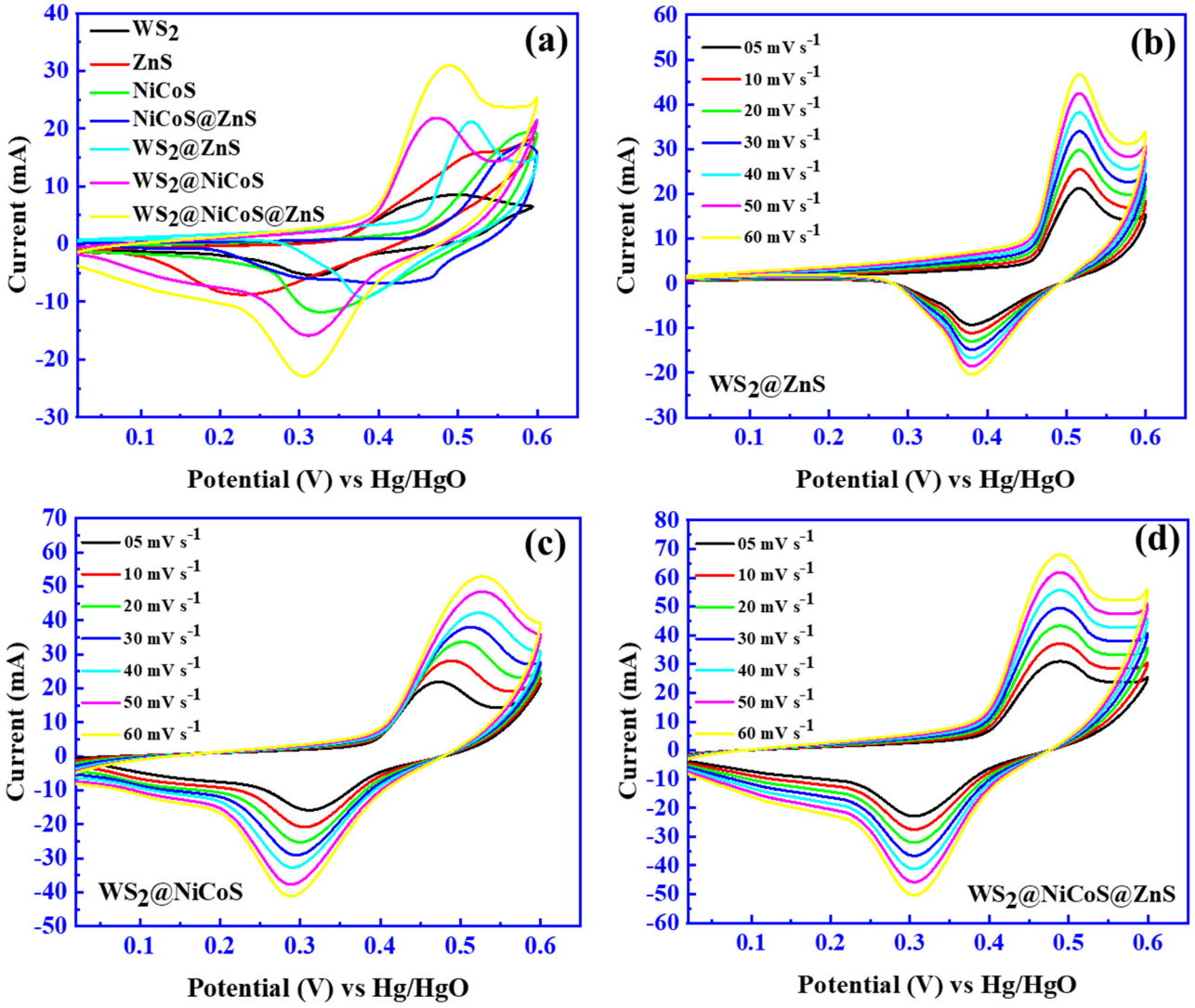


Figure 3. (**a**) Evaluation of the CV plots of all samples at 5 mV s^{-1}; (**b**) CV graphs of WS_2@ZnS; (**c**) WS_2@NiCoS; (**d**) WS_2@NiCoS@ZnS at various scan rates of 05 to 60 mV s^{-1}.

We also used GCD tests to see how much energy the electrode materials could store at room temperature, with a constant voltage ranging from 0 to 0.6 V and different current densities of 2.0 A g^{-1} to 3.0 A g^{-1}. Figure 4a displays the GCD plots of WS_2, ZnS, NiCoS, WS_2@ZnS, WS_2@NiCoS, and WS_2@NiCoS@ZnS using 1 M KOH electrolyte at 2 A g^{-1}. Figure 4b–d shows the CV curves of WS_2@ZnS, WS_2@NiCoS, and WS_2@NiCoS@ZnS,

respectively. The greater area under the curve, which indicates improved charge storage capacity, is seen in the comparative study of a CV of WS_2@NiCoS@ZnS material. The WS_2@NiCoS@ZnS shows highly preferable GCD results over other reference samples, as shown in Figure 4d. The improved performance of WS_2@NiCoS@ZnS in a 1.0 M KOH electrolyte solution is due to the increased ionic mobility and conductivity and the small hydrated ionic radii of KOH ions.

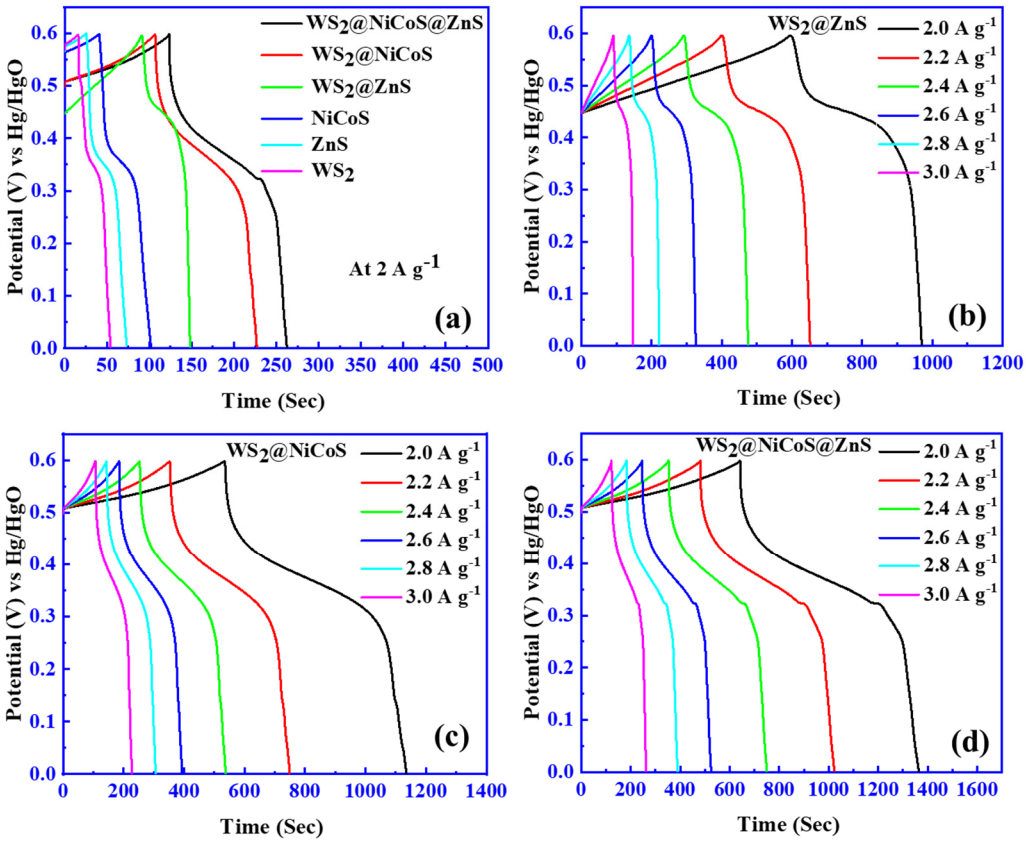


Figure 4. (**a**) The GCD curves comparison of all samples were obtained at 2 A g^{-1}. (**b**) GCD curves of WS_2@ZnS, (**c**) WS_2@NiCoS, and (**d**) WS_2@NiCoS@ZnS at 2 to 3 A g^{-1}.

The ability of the electrodes to store charge is indicated by their specific capacitance (Cs) and specific capacity (Qs), which are determined using the relationships provided below:

$$Q_s = \frac{1}{mv}\int_{V_i}^{V_f} (I \times V)\, dV \quad (1)$$

$$C_s = \frac{1}{mv\Delta V}\int_{V_i}^{V_f} (I \times V)\, dV \quad (2)$$

Herein, 'm' stands for loading mass, 'v' for scan rate, 'ΔV' for voltage, and the integral section implies the region encircled by the CV profile. These correlations show that Qs and Cs directly impact the area of a CV. When the scan rate increases, the peak currents increase due to the acceleration of faradaic reactions, and the Qs decrease because the reaction time is reduced. The electrode materials WS_2, ZnS, NiCoS, WS_2@ZnS, WS_2@NiCoS, and WS_2@NiCoS@ZnS are further studied electrochemically with 1 M KOH. The base reference materials WS_2, NiCoS, WS_2@ZnS, WS_2@NiCoS, and WS_2@NiCoS@ZnS delivered the maximum Q_s of 560.97 C g^{-1}, 695.61 C g^{-1}, 799.66 C g^{-1}, 942.81 C g^{-1}, and 1189.30 C g^{-1} at 5 mV s^{-1}, correspondingly, as shown in Figure 5a. The electrode with composite material WS_2@NiCoS performed better than the base materials as it provided a Q_s value of 942.81 C g^{-1} due to the complementary effects of NiCoS and WS_2. Finally,

cyclic voltammetry measurements are performed on the NiCoS@ZnS doped with WS_2 nanosheets. The sample with the highest Qs value, 1189.30 C g^{-1}, was the electrode with WS_2 doped material. Due to the abundance of active sites made accessible for faradaic reactions by WS_2 nanosheets, the higher Qs are the outcome. The improved electroconductivity of the electrode resulted from the increased adhesion of NiCoS@ZnS to WS_2 nanosheets, which opened up more pathways for electron transport. Results for specific capacitance (Cs), as determined by Equation (2). The Cs of WS_2, NiCoS, WS_2@ZnS, WS_2@NiCoS, and WS_2@NiCoS@ZnS are claimed to be 934.95 C g^{-1}, 1159.35 C g^{-1}, 1332.76 C g^{-1}, 1571.35, and 1982.16 C g^{-1} at 5 mV s^{-1} is represented in Supplementary Information Figure S4a.

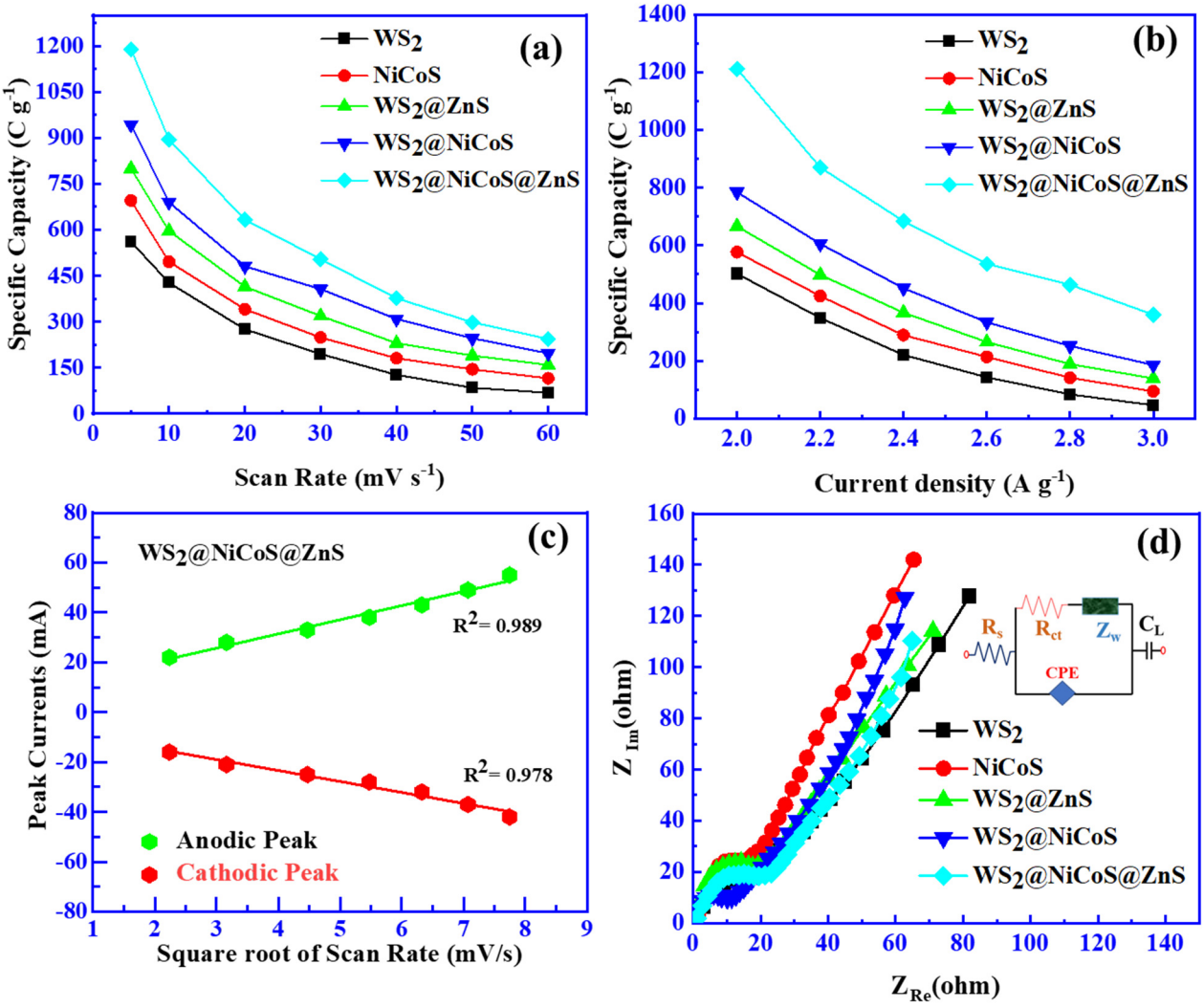


Figure 5. (**a**) Display the Qs of WS_2, NiCoS, WS_2@ZnS, WS_2@NiCoS, and WS_2@NiCoS@ZnS at various scans takes 5 to 60 mV s^{-1}. (**b**) The Qs of WS_2, NiCoS, WS_2@ZnS, WS_2@NiCoS, and WS_2@NiCoS@ZnS at versus current density (2 to 3 A g^{-1}). (**c**) Anodic peak and cathodic peak currents of the WS_2@NiCoS@ZnS composite. (**d**) EIS analysis and equivalent circuit of all samples.

The nonlinearity of the GCD profiles with a little hump and their uniformity reveals that the material is of battery-grade quality, which is shown by the reversibility of the faradaic reactions and subsequent CV results. As we increase the current density value, the discharge time reduces, reducing the time available for the faradaic processes. This reduction in discharge duration diminishes the electrode's capacity to store charge. The Qs

and Cs, which are calculated using the supplied relations below, determine the capacity to store charge:

$$Q_s = \frac{I \times \Delta t}{m} \quad (3)$$

$$C_s = \frac{I \times \Delta t}{m \times \Delta V} \quad (4)$$

where 'm' stands for loaded mass on Ni foam, 'Δt' for discharging time (Sec), and 'ΔV' for the operating voltage. The Q_s values of WS_2, NiCoS, WS_2@ZnS, WS_2@NiCoS, and WS_2@NiCoS@ZnS delivered the maximum Q_s are 502.24 C g^{-1}, 576.82 C g^{-1}, 666.38 C g^{-1}, 784.38 C g^{-1}, and 1211.58 C g^{-1} at 2 A g^{-1}, respectively, as shown in Figure 5b. When WS_2 nanosheets were added to the NiCoS@ZnS electrode material, the electrode demonstrated superior electrochemical performance during testing. At 2 A g^{-1}, the WS_2-doped NiCoS@ZnS had an exceptional Qs value of 1211.58 C g^{-1}. The GCD-related Cs values trend of WS_2, NiCoS, WS_2@ZnS, WS_2@NiCoS and WS_2@NiCoS@ZnS are claimed to be 934.95 F g^{-1}, 1159.35 F g^{-1}, 1332.76 F g^{-1}, 1571.35 F g^{-1} and 1982.16 F g^{-1} at 5 mV s^{-1} is represented in Supplementary data as a bar graph showing Figure S4b. Anodic peak current and cathodic peak current refer to the electrochemical behavior of a material in CV experimentation. WS_2@NiCoS@ZnS is a composite material composed of tungsten disulfide (WS_2) coated with nickel cobalt sulfide (NiCoS) and further coated with zinc sulfide (ZnS). The anodic peak current typically corresponds to the oxidation process (loss of electrons), while the cathodic current corresponds to the reduction process (gain of electrons). We can see here that when the scan rate (SR) increases, the anodic current also increases. The maximum calculated current values of the Anodic and cathodic peaks are 55 mA and −42 mA, as shown in Figure 5c.

The conductivity and capacity to store charge of the WS_2, NiCoS, WS_2@ZnS, WS_2@NiCoS@, and WS_2@NiCoS@ZnS electrodes were compared by performing EIS. Where the real and imaginary axes meet at higher frequencies is the electrode materials' equivalent series resistance (ESR). The ESR governs the conductivity of the electrode material. More resistance indicates a higher ESR value and vice versa. Figure 5d shows the material's equivalent ESR value determined using EIS. This proves that WS_2@NiCoS@ZnS has the lowest value among the other samples. There is no sample with a lower equivalent series resistance value than WS_2@NiCoS@ZnS. The unique microporous design of the composite allows it to have synergistic effects, leading to decreased charge transfer resistance.

Additionally, the materials are examined for their potential applications by conducting electrochemical tests using a two-electrode setup. To achieve this, we use Whatman filter paper as a dielectric medium to separate the cathode and anode electrodes, and we combine active materials (WS_2@ZnS, WS_2@NiCoS, and WS_2@NiCoS@ZnS) with activated carbon (AC) chips. A schematic representation of the setup device is shown in Figure 6a. The electrochemical data indicate that the combination of the battery and supercapacitor grade electrodes' faradic and capacitive behaviors results in a higher energy storage capacity for the device. Redox processes allow battery-grade electrodes to store large amounts of energy; in contrast, supercapacitor-grade electrodes store charge by absorbing and desorbing charges.

The electrochemical performance of WS_2@NiCoS@ZnS was assessed using a CV investigation using a three-electrode setup and a scan rate of 5 mV s^{-1}. Figure 6b illustrates the virtually rectangular curves of the capacitive-type electrode and the redox peaks of the battery-type electrode. The high-performance WS_2@NiCoS@ZnS//AC asymmetric device's cyclic voltammograms were recorded at 5 mV s^{-1} to 50 mV s^{-1} across a wide voltage range of 0 to 1.6 V are shown in Figure 6c. Quasi-rectangular curves in the coupled electrodes' CV show the existence of both kinds of processes. Moreover, increasing the scanning speed does not affect the CV's form, indicating its high-rate capacity and stability.

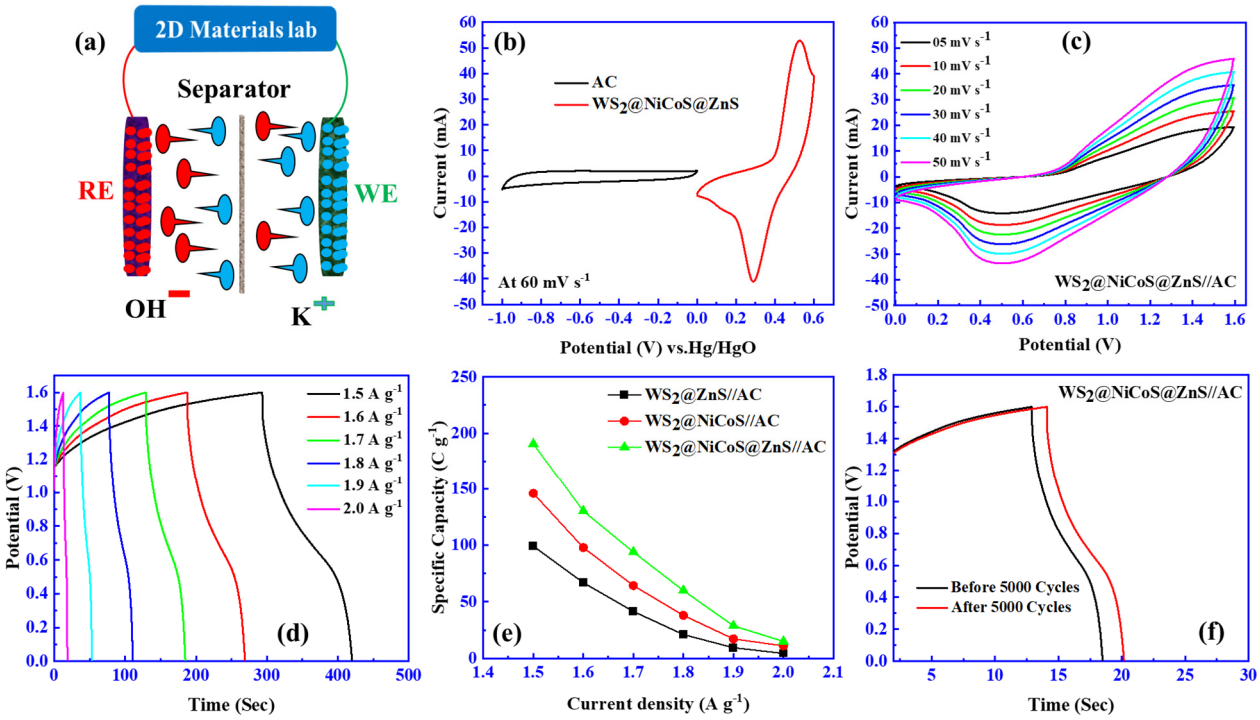


Figure 6. (**a**) The construction and design of an asymmetric device. (**b**) The CV investigation of AC and WS_2@NiCoS@ZnS using a 3-electrode arrangement and a scan rate of 5 mV s^{-1}. (**c**) CV analysis was used to investigate the characteristics of WS_2@NiCoS@ZnS//AC at 5 to 50 mV s^{-1}. (**d**) Display GCD curves of supercapattery device at different current densities from 1.5 A g^{-1} to 2 A g^{-1}. (**e**) The Qs vs. current density of WS_2@ZnS//AC, WS_2@NiCoS//AC, and WS_2@NiCoS@ZnS//AC are shown in a comparative plot. (**f**) The device stability was shown before and after 5000 GCD cycles.

Similarly, the supercapattery (WS_2@NiCoS@ZnS//AC) is subjected to GCD cycles at various current densities (1.5 to 2.0 A g^{-1}) and potential window (PW) of 0–1.6 V, as shown in Figure 6d. The Q_s of WS_2@ZnS//AC, WS_2@NiCoS//AC, and WS_2@NiCoS@ZnS//AC at 1.5 to 2.0 A g^{-1} values are 99.17 C g^{-1}, 145.93 C g^{-1}, and 190.5 C g^{-1}, given in Figure 6e. The decrease in Qs value when the current densities are increased is due to the reduced time for ions to interact with the active material. The homogeneous distribution of NiCoS@ZnS on WS_2, the special porous structure of the composite, which offers more active sites for charge storage, is responsible for the device's exceptional performance. Supplementary data in Figure S5 show a bar graph to calculate the specific capacitance values for each of the other three devices as WS_2@ZnS//AC, WS_2@NiCoS//AC, and WS_2@NiCoS@ZnS//AC. Here, WS_2@NiCoS@ZnS//AC is operated for 5000 GCD cycles at 2.0 A g^{-1}. The device stability before and after 5000 GCD cycles is shown in Figure 6f.

The cyclic stability of the device is a significant aspect of its functioning. Figure 7a also displays the GCD duration for 5000 cycles. This discovery proves that the WS_2@NiCoS@ZnS//AC synergy can withstand the negative aspects of both materials. The supercapacitor device's coulombic efficiency and capacity retention, shown in Figure 7b as final values after 5000 GCD cycles, are 93.23% and 85.19%, respectively.

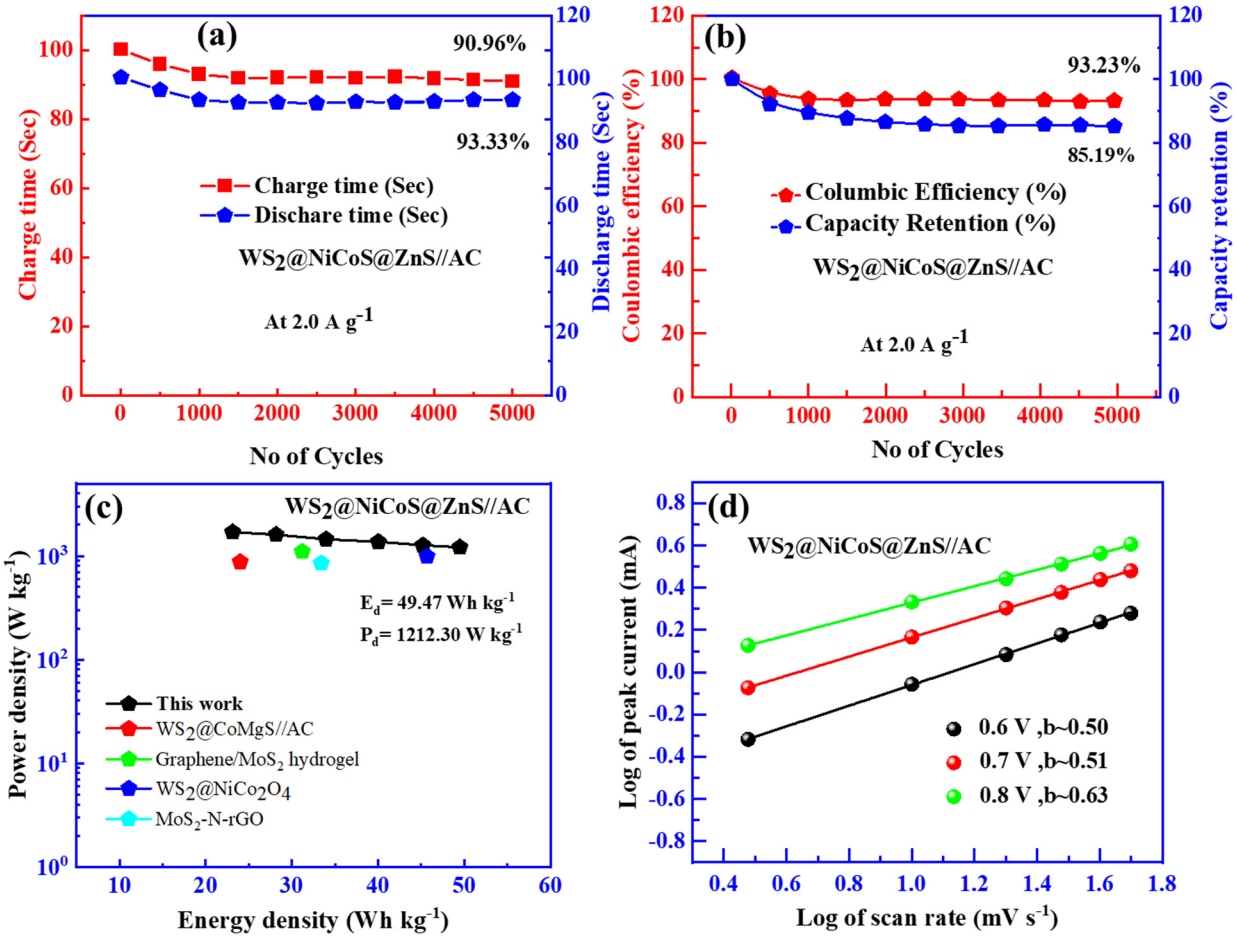


Figure 7. (**a**) After 5000 cycles, the charge/discharge measurements and cycling stability of WS_2@NiCoS@ZnS//AC are assessed. (**b**) Columbic efficiency and capacity retention observations after 5000 cycles. (**c**) Comparing WS_2@NiCoS@ZnS//AC with previously published work, a graph is shown the E_d and P_d. (**d**) A graph is used to show the calculation of the b-values, which are based on the linear curve.

The electrochem supercapattery device may be best understood by analyzing its energy density (E_d) and power density (P_d). Using the provided relations, we can calculate these values for the present assembly [28]:

$$E_d\left(\text{Wh kg}^{-1}\right) = \frac{Q_s \times \Delta V}{7.2} \quad (5)$$

$$P_d\left(\text{W kg}^{-1}\right) = \frac{E \times 3600}{\Delta t} \quad (6)$$

Here, 'Δt' denotes the discharge time, and 'ΔV' represents the voltage range. With an outstanding P_d value of 1212.30 W kg^{-1}, the most significant E_d value is 49.47 W h kg^{-1}. The t E_d and P_d results are compared with published data in Figure 7c. The WS_2@NiCoS@ZnS//AC is now recognized as a high-performance supercapattery grade material because of these outstanding findings. The peak current values log against the scanning rate log in Figure 7d. The electrode material's b-value determines whether it is categorized as a supercapacitor battery or supercapattery. The battery-grade composite electrode material's b-values fall between 0.0 and 0.5; supercapacitor-grade material is found in the b-values between 0.8 and 1, and supercapattery material is found in the b-values between 0.5 and 0.8 [59]. The b-values for the WS_2@NiCoS@ZnS//AC device support our claim that we have successfully manufactured a supercapattery.

Photochemical Activity

The fundamental workings of the photochemical cell are shown in Figure 8a. The Supplementary Materials include information on the experimental setup, including details and parameters [60,61]. The amperometrically resulting photocurrent was identified in a current versus time profile at chopping illumination settings at open circuit potential (OCP) with frequent on/off cycles, as shown in Figure 8b. Excellent photo-switching performance was achieved by WS_2@NiCoS@ZnS photoelectrode because of its quick response, recovery times, and strong photoactivity. Light illumination begins with the presence of a strong point, which allows the charge separation procedure to be successful. Stable photocurrent starts with an exponential drop. WS_2@NiCoS@ZnS may, thus, be used as a successful photoelectrocatalyst with a better knowledge of adhesion properties on the photoelectrode surface.

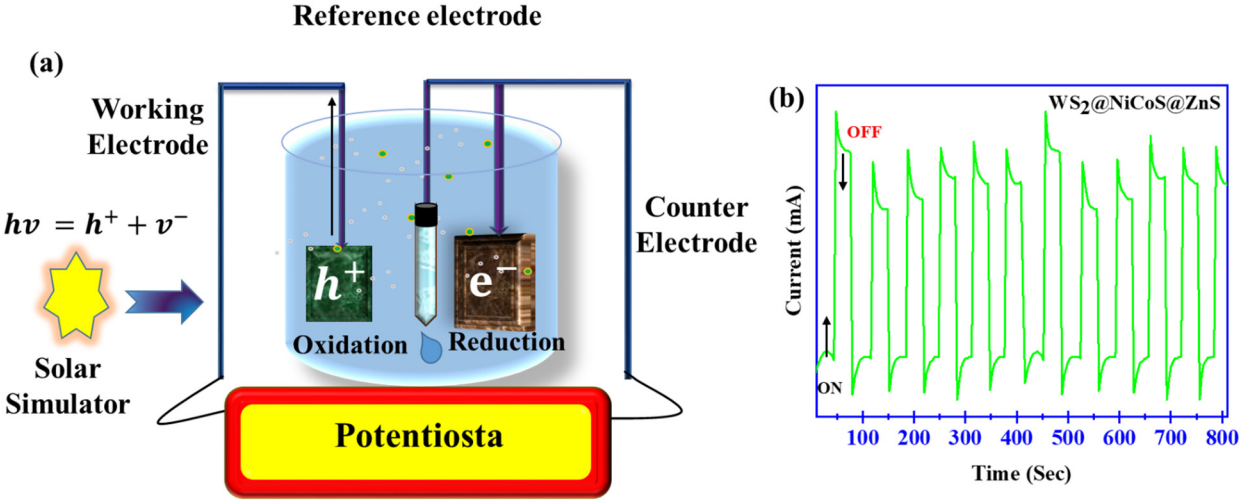


Figure 8. (**a**) Diagram illustrating the essential operation of a photoelectrochemical system. (**b**) A photocurrent–time profile under chopped light (On/Off) conditions was generated for the WS_2@NiCoS@ZnS photoelectrode using simulated solar light.

5. Conclusions

In short, we used the hydrothermal technique to synthesize the NiCoS@ZnS, and we obtained the WS_2 nanosheets by tip-sonicating the WS_2 nanopowder. SEM makes it possible to observe that the NiCoS@ZnS nanoparticles are implanted on WS_2 nanosheets as a consequence of doping. To investigate the morphology, structure, and composition of the doped material, further structural analysis methods such as XRD, BET, and XPS spectroscopy are used. CV, GCD, and EIS provide a thorough electrochemical investigation of the doped and undoped materials using a three-electrode setup. The sample of NiCoS@ZnS doped with WS_2 nanosheets produced a minimal equivalent series resistance of 3.1 Ω and a good Qs of 1211.58 C g^{-1} or 2019.3 F g^{-1} at 1.8 Ag^{-1} when using an electrolyte solution of 1 M KOH. Following that, two electrode assemblies are used to practically analyze the exceptional properties of WS_2@NiCoS@ZnS. An asymmetric device using the WS_2@NiCoS@ZnS//AC electrode has a high specific capacity of 190.5 C g^{-1} due to the combined influence of both electrode materials. After 5000 consecutive cycles at 2.0 A g^{-1}, this equates to 49.47 Wh kg^{-1} E_d and 1212.30 W kg^{-1} P_d. The remarkable electrochemical outcomes suggest that WS_2@NiCoS@ZnS is a promising material for enhancing energy storage apparatuses.

Supplementary Materials: The following supporting information can be downloaded at: https://www.mdpi.com/article/10.3390/cryst14110916/s1, Figure S1: BET analysis of WS_2@ZnS, and WS_2@NiCoS nanocomposite material; Figure S2: XPS analysis of nanocomposite; Figure S3: CV graphs of

NiCoS@ZnS; Figure S4: Specific capacitance of all the samples at scan rate of 5 mV/s; Figure S5: The specific capacitance of WS_2@ZnS//AC hybrid device.

Author Contributions: Methodology, M.I. and M.W.I.; software, M.I.; formal analysis, A.M.A., A.S.A. and S.M.; data curation, A.S.A. and S.M.; writing—original draft, A.M.A.; writing—review and editing, M.I., A.S.A. and M.W.I.; supervision, A.M.A. All authors have read and agreed to the published version of the manuscript.

Funding: The authors declare that no funds or grants were received during the preparation of this manuscript.

Data Availability Statement: Data is contained within the article or Supplementary Materials.

Acknowledgments: The authors appreciate Princess Nourah bint Abdulrahman University Researchers Supporting Project number (PNURSP2024R479), Princess Nourah bint Abdulrahman University, Riyadh, Saudi Arabia.

Conflicts of Interest: The authors declare no conflict of interest.

References

1. Xu, X.; Dong, Y.; Hu, Q.; Si, N.; Zhang, C. Electrochemical hydrogen storage materials: State-of-the-art and future perspectives. *Energy Fuels* **2024**, *38*, 7579–7613. [CrossRef]
2. Sheikh, Z.A.; Vikraman, D.; Kim, H.; Aftab, S.; Shaikh, S.F.; Shahzad, F.; Jung, J.; Kim, H.S.; Hussain, S.; Kim, D.K. Perovskite oxide-based nanoparticles embedded MXene composites for supercapacitors and oxygen evolution reactions. *J. Energy Storage* **2024**, *81*, 110342. [CrossRef]
3. Yang, F.; Feng, X.; Glans, P.-A.; Guo, J. MoS_2 for beyond lithium-ion batteries. *APL Mater.* **2021**, *9*, 050903. [CrossRef]
4. Chatterjee, D.P.; Nandi, A.K. A review on the recent advances in hybrid supercapacitors. *J. Mater. Chem. A* **2021**, *9*, 15880–15918. [CrossRef]
5. Hussain, S.; Vikraman, D.; Mehran, M.T.; Hussain, M.; Nazir, G.; Patil, S.A.; Kim, H.-S.; Jung, J. Ultrasonically derived WSe_2 nanostructure embedded MXene hybrid composites for supercapacitors and hydrogen evolution reactions. *Renew. Energy* **2022**, *185*, 585–597. [CrossRef]
6. Vikraman, D.; Hussain, S.; Abbas, Z.; Karuppasamy, K.; Kang, W.-S.; Santhoshkumar, P.; Kathalingam, A.; Jung, J.; Kim, H.-S. Exploring the experimental study and density functional theory calculations of symmetric and asymmetric chalcogen atoms interacted molybdenum dichalcogenides for lithium-ion batteries. *J. Mater. Sci. Technol.* **2023**, *162*, 44–56. [CrossRef]
7. Vikraman, D.; Hussain, S.; Rabani, I.; Feroze, A.; Ali, M.; Seo, Y.-S.; Chun, S.-H.; Jung, J.; Kim, H.-S. Engineering $MoTe_2$ and Janus SeMoTe nanosheet structures: First-principles roadmap and practical uses in hydrogen evolution reactions and symmetric supercapacitors. *Nano Energy* **2021**, *87*, 106161. [CrossRef]
8. Vikraman, D.; Hussain, S.; Karuppasamy, K.; Feroze, A.; Kathalingam, A.; Sanmugam, A.; Chun, S.-H.; Jung, J.; Kim, H.-S. Engineering the novel $MoSe_2$-Mo_2C hybrid nanoarray electrodes for energy storage and water splitting applications. *Appl. Catal. B Environ.* **2020**, *264*, 118531. [CrossRef]
9. Zeng, K.; Zhang, D. Recent progress in alkaline water electrolysis for hydrogen production and applications. *Prog. Energy Combust. Sci.* **2010**, *36*, 307–326. [CrossRef]
10. Wang, J.; Liu, Z.; Zhan, C.; Zhang, K.; Lai, X.; Tu, J.; Cao, Y. 3D hierarchical NiS_2/MoS_2 nanostructures on CFP with enhanced electrocatalytic activity for hydrogen evolution reaction. *J. Mater. Sci. Technol.* **2020**, *39*, 155–160. [CrossRef]
11. Chhowalla, M.; Shin, H.S.; Eda, G.; Li, L.-J.; Loh, K.P.; Zhang, H. The chemistry of two-dimensional layered transition metal dichalcogenide nanosheets. *Nat. Chem.* **2013**, *5*, 263–275. [CrossRef] [PubMed]
12. Wei, C.; Liu, C.; Gao, L.; Sun, Y.; Liu, Q.; Zhang, X.; Guo, J. MoS_2 nanosheets decorated $Ni(OH)_2$ nanorod array for active overall water splitting. *J. Alloys Compd.* **2019**, *796*, 86–92. [CrossRef]
13. Ling, Y.; Kazim, F.M.; Ma, S.; Zhang, Q.; Qu, K.; Wang, Y.; Xiao, S.; Cai, W.; Yang, Z. Strain induced rich planar defects in heterogeneous WS_2/WO_2 enable efficient nitrogen fixation at low overpotential. *J. Mater. Chem. A* **2020**, *8*, 12996–13003. [CrossRef]
14. Yan, R.; Wang, J.; He, S.; Huang, L.; Wang, B.; Zhu, M.; Hu, S. Quasi-solid-state silicon-air batteries with high capacities and wide-temperature adaptabilities. *Energy Storage Mater.* **2024**, *71*, 103656. [CrossRef]
15. Ji, L.; Cao, H.; Xing, W.; Liu, S.; Deng, Q.; Shen, S. Facilitating electrocatalytic hydrogen evolution via multifunctional tungsten@ tungsten disulfide core–shell nanospheres. *J. Mater. Chem. A* **2021**, *9*, 9272–9280. [CrossRef]
16. Dai, J.; Luo, L.; Tang, Z.; Lv, Y.; Xie, H.; Zuo, H.; Yang, C.; Wang, X.; Fan, M.; Xu, Y. Strategy for constructing highly stable supercapacitors: Channeling of thin-layer polyaniline to enhance pseudo-capacitance of the CuS/polyaniline@ MoS_2 composites. *Compos. Sci. Technol.* **2022**, *219*, 109240. [CrossRef]
17. Wang, M.; Zhang, L.; Huang, M.; Zhang, Q.; Zhao, X.; He, Y.; Lin, S.; Pan, J.; Zhu, H. One-step synthesis of a hierarchical self-supported WS_2 film for efficient electrocatalytic hydrogen evolution. *J. Mater. Chem. A* **2019**, *7*, 22405–22411. [CrossRef]
18. Chen, Y.; Zhang, X.; Qin, J.; Liu, R. Taming the challenges of activity and selectivity in catalysts for electrochemical N_2 fixation via single metal atom supported on WS_2. *Appl. Surf. Sci.* **2022**, *571*, 151357. [CrossRef]

19. Vikraman, D.; Hussain, S.; Karuppasamy, K.; Kathalingam, A.; Jo, E.-B.; Sanmugam, A.; Jung, J.; Kim, H.-S. Engineering the active sites tuned MoS_2 nanoarray structures by transition metal doping for hydrogen evolution and supercapacitor applications. *J. Alloys Compd.* **2022**, *893*, 162271. [CrossRef]
20. Wang, H.; Shu, T.; Lin, C.; Sun, F.; Wang, Z.; Lin, B.; Wei, F.; Yao, K.X.; Qi, J.; Sui, Y. Hierarchical construction of Co_3S_4 nanosheet coated by 2D multi-layer MoS_2 as an electrode for high performance supercapacitor. *Appl. Surf. Sci.* **2022**, *578*, 151897. [CrossRef]
21. Yuan, P.; Xue, R.; Wang, Y.; Su, Y.; Zhao, B.; Wu, C.; An, W.; Zhao, W.; Ma, R.; Hu, D. Horizontally-oriented barium titanate@ polydomine/polyimide nanocomposite films for high-temperature energy storage. *J. Colloid Interface Sci.* **2024**, *662*, 1052–1062. [CrossRef] [PubMed]
22. Wang, Y.; Song, Y.; Xia, Y. Electrochemical capacitors: Mechanism, materials, systems, characterization and applications. *Chem. Soc. Rev.* **2016**, *45*, 5925–5950. [CrossRef] [PubMed]
23. Lin, Z.; Goikolea, E.; Balducci, A.; Naoi, K.; Taberna, P.-L.; Salanne, M.; Yushin, G.; Simon, P. Materials for supercapacitors: When Li-ion battery power is not enough. *Mater. Today* **2018**, *21*, 419–436. [CrossRef]
24. Iqbal, M.Z.; Khan, J.; Awan, H.T.A.; Alzaid, M.; Afzal, A.M.; Aftab, S. Cobalt–manganese-zinc ternary phosphate for high performance supercapattery devices. *Dalton Trans.* **2020**, *49*, 16715–16727. [CrossRef]
25. Iqbal, M.Z.; Khan, J. Optimization of cobalt-manganese binary sulfide for high performance supercapattery devices. *Electrochim. Acta* **2021**, *368*, 137529. [CrossRef]
26. Wei, B.; Liang, H.; Wang, R.; Zhang, D.; Qi, Z.; Wang, Z. One-step synthesis of graphitic-C_3N_4/ZnS composites for enhanced supercapacitor performance. *J. Energy Chem.* **2018**, *27*, 472–477. [CrossRef]
27. Gao, L.; Cao, M.; Zhang, C.; Li, J.; Zhu, X.; Guo, X.; Toktarbay, Z. Zinc selenide/cobalt selenide in nitrogen-doped carbon frameworks as anode materials for high-performance sodium-ion hybrid capacitors. *Adv. Compos. Hybrid Mater.* **2024**, *7*, 1–11. [CrossRef]
28. Rauf, M.; Shah, S.S.; Shah, S.K.; Shah, S.N.A.; Haq, T.U.; Shah, J.; Ullah, A.; Ahmad, T.; Khan, Y.; Aziz, M. Facile hydrothermal synthesis of zinc sulfide nanowires for high-performance asymmetric supercapacitor. *J. Saudi Chem. Soc.* **2022**, *26*, 101514. [CrossRef]
29. Chameh, B.; Moradi, M.; Kaveian, S. Synthesis of hybrid ZIF-derived binary ZnS/CoS composite as high areal-capacitance supercapacitor. *Synth. Met.* **2020**, *260*, 116262. [CrossRef]
30. Wang, X.; Tian, L.; Long, X.; Yang, M.; Song, X.; Xie, W.; Liu, D.; Fu, Y.; Li, J.; Li, Y. Cracked bark-inspired ternary metallic sulfide ($NiCoMnS_4$) nanostructure on carbon cloth for high-performance aqueous asymmetric supercapacitors. *Sci. China Mater.* **2021**, *64*, 1632–1641. [CrossRef]
31. Iqbal, M.Z.; Khan, J.; Afzal, A.M.; Aftab, S. Exploring the synergetic electrochemical performance of cobalt sulfide/cobalt phosphate composites for supercapattery devices with high-energy and rate capability. *Electrochim. Acta* **2021**, *384*, 138358. [CrossRef]
32. Choudhary, N.; Li, C.; Chung, H.-S.; Moore, J.; Thomas, J.; Jung, Y. High-performance one-body core/shell nanowire supercapacitor enabled by conformal growth of capacitive 2D WS_2 layers. *ACS Nano* **2016**, *10*, 10726–10735. [CrossRef]
33. Eftekhari, A. Tungsten dichalcogenides (WS_2, WSe_2, and WTe_2): Materials chemistry and applications. *J. Mater. Chem. A* **2017**, *5*, 18299–18325. [CrossRef]
34. Cherusseri, J.; Choudhary, N.; Kumar, K.S.; Jung, Y.; Thomas, J. Recent trends in transition metal dichalcogenide based supercapacitor electrodes. *Nanoscale Horiz.* **2019**, *4*, 840–858. [CrossRef]
35. Mohan, V.V.; Manuraj, M.; Anjana, P.M.; Rakhi, R.B.J.E.T. WS_2 nanoflowers as efficient electrode materials for supercapacitors. *Energy Technol.* **2022**, *10*, 2100976. [CrossRef]
36. Gupta, H.; Chakrabarti, S.; Mothkuri, S.; Padya, B.; Rao, T.; Jain, P. High performance supercapacitor based on 2D-MoS_2 nanostructures. *Mater. Today Proc.* **2020**, *26*, 20–24. [CrossRef]
37. Elías, A.L.; Perea-López, N.; Castro-Beltrán, A.; Berkdemir, A.; Lv, R.; Feng, S.; Long, A.D.; Hayashi, T.; Kim, Y.A.; Endo, M. Controlled synthesis and transfer of large-area WS_2 sheets: From single layer to few layers. *ACS Nano* **2013**, *7*, 5235–5242. [CrossRef]
38. Krishna, T.; Himasree, P.; Raghavendra, K.; Rao, S.S.; Kundakarla, N.B.; Punnoose, D.; Kim, H. Hydrothermal synthesis of layered CoS@WS_2 nanocomposite as a potential electrode for high-performance supercapacitor applications. *J. Mater. Sci. Mater. Electron.* **2020**, *31*, 16290–16298. [CrossRef]
39. Shrivastav, V.; Sundriyal, S.; Goel, P.; Shrivastav, V.; Tiwari, U.K.; Deep, A. ZIF-67 derived Co_3S_4 hollow microspheres and WS_2 nanorods as a hybrid electrode material for flexible 2V solid-state supercapacitor. *Electrochim. Acta* **2020**, *345*, 136194. [CrossRef]
40. Thiehmed, Z.; Shakoor, A.; Altahtamouni, T. Recent advances in WS_2 and its based heterostructures for water-splitting applications. *Catalysts* **2021**, *11*, 1283. [CrossRef]
41. Štengl, V.; Tolasz, J.; Popelková, D. Ultrasonic preparation of tungsten disulfide single-layers and quantum dots. *RSC Adv.* **2015**, *5*, 89612–89620. [CrossRef]
42. Ali, Y.; Nguyen, V.-T.; Nguyen, N.-A.; Shin, S.; Choi, H.-S. Transition-metal-based NiCoS/C-dot nanoflower as a stable electrocatalyst for hydrogen evolution reaction. *Int. J. Hydrogen Energy* **2019**, *44*, 8214–8222. [CrossRef]
43. Zhang, S.; Ren, J.; Gu, T.; Guo, H.; Wang, H.; Imran, M.; Ren, R.-P.; Lv, Y.-K. Porous NiCoS nanosheets decorated activated carbon cloth for flexible asymmetric supercapacitors. *Diam. Relat. Mater.* **2022**, *127*, 109154. [CrossRef]

44. Imran, M.; Waris, M.H.; Khan, R.; Afzal, A.M.; Iqbal, M.W.; Mumtaz, M.A.; Ghfar, A.A.; Ali, A.; Mumtaz, S.; Hussain, Z. High-performance energy storage hybrid supercapacitor device based on NiCoS@ CNT@ graphene composite electrode material. *Phys. Scr.* **2023**, *98*, 115981. [CrossRef]
45. Qin, Y.; Peng, Y.; Yang, W.; Wang, Y.; Cui, J.; Zhang, Y. Ultrathin exfoliated WS_2 nanosheets in low-boiling-point solvents for high-efficiency hydrogen evolution reaction. In *IOP Conference Series: Materials Science and Engineering*; IOP Publishing: Bristol, UK, 2020; p. 012079.
46. Wang, G.; Geng, B.; Huang, X.; Wang, Y.; Li, G.; Zhang, L. A convenient ultrasonic irradiation technique for in situ synthesis of zinc sulfide nanocrystallites at room temperature. *Appl. Phys. A* **2003**, *77*, 933–936. [CrossRef]
47. Pal, S.; Dutta, S.; De, S. Synthesis of MoS_2/rGO nanosheets hybrid materials for enhanced visible light assisted photocatalytic activity. In *AIP Conference Proceedings*; AIP Publishing: Melville, NY, USA, 2018; p. 050129.
48. Kumar, Y.A.; Mani, G.; Pallavolu, M.R.; Sambasivam, S.; Nallapureddy, R.R.; Selvaraj, M.; Alfakeer, M.; Bahajjaj, A.A.A.; Ouladsmane, M.; Rao, S.S.; et al. Facile synthesis of efficient construction of tungsten disulfide/iron cobaltite nanocomposite grown on nickel foam as a battery-type energy material for electrochemical supercapacitors with superior performance. *J. Colloid Interface Sci.* **2022**, *609*, 434–446. [CrossRef]
49. Zhou, Y.; Duan, R. Leak-Proof Reversible Thermochromic Microcapsule Phase Change Materials with High Latent Thermal Storage for Thermal Management. *ACS Appl. Energy Mater.* **2024**, *7*, 5944–5956. [CrossRef]
50. Yuan, P.; Southon, P.D.; Liu, Z.; Green, M.E.; Hook, J.M.; Antill, S.J.; Kepert, C.J. Functionalization of halloysite clay nanotubes by grafting with γ-aminopropyltriethoxysilane. *J. Phys. Chem. C* **2008**, *112*, 15742–15751. [CrossRef]
51. Imran, M.; Iqbal, M.W.; Afzal, A.M.; Faisal, M.M.; Alzahrani, H. Synergetic electrochemical performance of Nix–Mnx sulfide-based binary electrode material for supercapattery devices. *J. Appl. Electrochem.* **2023**, *53*, 1125–1136. [CrossRef]
52. Choi, S.H.; Boo, S.J.; Lee, J.-H.; Kang, Y.C. Electrochemical properties of tungsten sulfide–carbon composite microspheres prepared by spray pyrolysis. *Sci. Rep.* **2014**, *4*, 5755. [CrossRef]
53. Zeng, P.; Ji, X.; Su, Z.; Zhang, S. WS_2/gC_3N_4 composite as an efficient heterojunction photocatalyst for biocatalyzed artificial photosynthesis. *RSC Adv.* **2018**, *8*, 20557–20567. [CrossRef] [PubMed]
54. Li, Y.; Ding, L.; Yin, S.; Liang, Z.; Xue, Y.; Wang, X.; Cui, H.; Tian, J. Photocatalytic H_2 evolution on TiO_2 assembled with Ti_3C_2 MXene and metallic 1T-WS_2 as co-catalysts. *Nano-Micro Lett.* **2020**, *12*, 6. [CrossRef] [PubMed]
55. Qian, D.; Chen, J.; Luo, H.; Wang, F.; Hua, L. Electric current-induced directional slip of dislocation and grain boundary ordering. *Mater. Today Adv.* **2024**, *24*, 100530. [CrossRef]
56. Imran, M.; Qasam, K.; Safdar, S.; Afzal, A.M.; Iqbal, M.W.; Mumtaz, S.; Munnaf, S.A.; Habila, M.A.; Fatima, W.; Ahmad, Z. Hydrothermally synthesized CuNiS@CNTs composite electrode material for hybrid supercapacitors and non-enzymatic electrochemical glucose sensor. *J. Mater. Sci. Mater. Electron.* **2024**, *35*, 441. [CrossRef]
57. Hengne, A.M.; Samal, A.K.; Enakonda, L.R.; Harb, M.; Gevers, L.E.; Anjum, D.H.; Hedhili, M.N.; Saih, Y.; Huang, K.-W.; Basset, J.-M. Ni–Sn-supported ZrO_2 catalysts modified by indium for selective CO_2 hydrogenation to methanol. *ACS Omega* **2018**, *3*, 3688–3701. [CrossRef]
58. Carey, B.J.; Daeneke, T.; Nguyen, E.P.; Wang, Y.; Ou, J.Z.; Zhuiykov, S.; Kalantar-Zadeh, K. Two solvent grinding sonication method for the synthesis of two-dimensional tungsten disulphide flakes. *Chem. Commun.* **2015**, *51*, 3770–3773. [CrossRef]
59. Iqbal, M.Z.; Faisal, M.M.; Sulman, M.; Ali, S.R.; Alzaid, M. Facile synthesis of strontium oxide/polyaniline/graphene composite for the high-performance supercapattery devices. *J. Electroanal. Chem.* **2020**, *879*, 114812. [CrossRef]
60. Dey, K.K.; Jha, S.; Kumar, A.; Gupta, G.; Srivastava, A.K.; Ingole, P.P. Layered vanadium oxide nanofibers as impressive electrocatalyst for hydrogen evolution reaction in acidic medium. *Electrochim. Acta* **2019**, *312*, 89–99. [CrossRef]
61. Imran, M.; Muhammad, Z.; Muzafar, N.; Afzal, A.M.; Iqbal, M.W.; Mumtaz, S.; Munnaf, S.A.; Albaqami, M.D.; Ahmad, Z. Enhanced the electrochemical performance of CoMgS nanocomposite electrode with the doping of ZnO for supercapacitor-battery hybrid device and photochemical activity. *J. Appl. Electrochem.* **2024**, *54*, 1501–1515. [CrossRef]

Disclaimer/Publisher's Note: The statements, opinions and data contained in all publications are solely those of the individual author(s) and contributor(s) and not of MDPI and/or the editor(s). MDPI and/or the editor(s) disclaim responsibility for any injury to people or property resulting from any ideas, methods, instructions or products referred to in the content.